Self-assembled para-Nitroanaline polymeric thin films as highly efficient generators of second harmonic light.

Hugo Gonçalves[a], Marlene Lúcio[a], Paulo E Lopes[b], César Bernardo[a] Michael Belsley[b]

[1] Centre of Physics, University of Minho, Campus de Gualtar, 4710-057 Braga, Portugal
[2] Institute for Polymers and Composites/i3N, University of Minho, Guimarães, Portugal

Abstract: Intense well-polarized second harmonic light was generated by *para*-Nitroaniline self-assembled thin films in different polymeric host matrices. The large area films of the organic chromophore with micron thickness were produced using a modified version of capillary growth. Analysis of the generated second harmonic light indicates that the *para*-Nitroaniline molecules, which nominally crystalize in a centrosymmetric space group, were organized into structures with an appreciable second order susceptibility dominated by a single tensor element. Under the best conditions, the film's effective second order optical susceptibility is slightly greater than that of beta barium borate for incident light at 800nm. Generalizing this approach to a broad range of organic molecules with strong individual molecular second order nonlinear responses, but which ordinarily form centrosymmetric organic crystals, could open a new pathway for the fabrication of efficient thin film second harmonic light generators.

PACS: 42.65.-k Nonlinear optics**; 42.65.An** Optical susceptibility; hyperpolarizability, **42.65.Ky** Frequency conversion; harmonic generation; **42.70.Jk** Polymers and organics

Declarations of interest: none

1. Introduction

Over the past decades, scientists have sought strategies to enhance the nonlinear optical response of organic molecules and polymers and to incorporate them into assemblies with high optical and thermal stability, as well, as the good optical transparency needed for most practical applications[1–6]. More often than not, the large individual molecular first order hyperpolarizabilities of the developed organic chromophores are associated with large dipolar moments in the ground state leading to strong interactions between the constituent molecules in these assemblies and a tendency to assemble in head to tail centrosymmetric structures that preclude stable and strong macroscopic second order nonlinear optical responses[7,8].

The arrangement of the molecular building blocks within supramolecular structures has a marked effect on their physical properties[9]. The development of techniques for controlling the

spatial arrangement of the individual components of a composite material at the nanometer and micrometer scale is, therefore, crucial to the design and fabrication of advanced electronic, optical, and mechanical materials[7,10–12]. *para*-Nitroaniline (*p*Na) is an organic chromophore with an appreciable molecular hyperpolarizability (β)[13,14], often considered a model for organic donor-acceptor systems with strong second order molecular responses[15–17]. However, *p*Na molecules tend to arrange themselves in an antiparallel centrosymmetric fashion in the solid state, causing their individual even order molecular non-linearities to cancel, making the bulk SHG signal vanish. Various methods to prevent this alignment have been proposed, including the introducing of chiral substituents, aligning the chromophores by a strong externally applied electric field or confined within 1D nanostructures and host-guest complexes [18–24].

Our group has previously reported that electro-spun nanofibers embedded with *p*Na can be efficient generators of second harmonic light [4,21], well beyond what can be expected due to the breaking of centrosymmetry at the *p*Na bulk crystalline surfaces [4]. This implies that the electrospinning process is able to somehow break the nominal centrosymmetry of the *p*Na embedded in the polymeric fibers. One possibility is that the strong DC electric field applied to eject the jet in the electro-spinning process induces subtle distortions into the *p*Na nanocrystals, or provokes a local polarization of the surrounding polymer which is then frozen into the fiber as it rapidly solidifies. To test whether the electric field is an essential stimulus for obtaining strong second harmonic responses we explore here growing *p*Na together with various polymers in a confined geometry. We have found that *p*Na thin films with a high SHG response can be cast using a series of linear aliphatic polymers with different molecular weights and with varying degrees of crystallinity; from amorphous to semi-crystalline. These films were obtained using a variation of capillary growth, by placing a precusrsor polymer *p*Na solution between the surfaces of two closely spaced glass slides. That is instead of restricting the *p*Na nanocrystals geometries by the physical dimensions of the ejected polymer jet in electro-spinning, the self-assembly of *p*Na crystals is restricted to the limited space on the order of a micron between the glass slides.

We have characterized the SHG response of the resulting thins films. For polymers with sufficient length, their inherent flexibility is the key factor determining the organization of the resulting *p*Na thin films. Two distinct co-crystallization mechanisms were observed. Long chain polymers, tended to produce largely continuous planar *p*Na films, whereas shorter polymer chains gave rise to dendritic arrangements. These different assemblies lead to different second harmonic responses as well as notable differences in the respective Raman spectra.

2. Experimental Section

Methods

Para-Nitroaniline (*p*Na) was purchased from Sigma Chemical Co and used as received. Polystyrene (PS) with a molecular weight (M_W 300000) was purchased from Alfa Aesar. Both Poly(hexano-6-lactone) (PCL) with (M_W 80000) and Poly(methyl methacrylate) (PMMA) with medium (M_W 120000) and low (M_W 15000) molecular weights were acquired from Sigma Chemical Co. The polymeric raw materials were dissolved in toluene ($C_6H_5CH_3$, 99.8%), purchased from Sigma-Aldrich. The prepared solution was stirred for several hours under ambient conditions. *p*Na in powder form was subsequently added to the polymeric solution, in a ratio of 2:1 polymer to *p*Na by weight, together with a few drops of acetone to aid solvation. The respective polymeric solutions with a concentration 10 wt% were deposited on glass microscope slides. The deposited solutions were covered with thin glass coverslips. The growth of the films was a slow process, occurring over several days.

Thin film fabrication

The thin films studied are quasi two-dimensional systems, with a thickness slightly greater than one micron, produced under ambient conditions at a constant temperature. In this approach the growth of the *p*Na films is geometrically restricted to the narrow gap between the two glass slides, similar to the capillarity growth process reported in the literature[25,26], see figure 1. The resulting *p*Na/polymeric thin films become visible to the naked eye after a few days. However, they continuously grow as long as some residual mobility in the polymeric matrix exists, that is until complete evaporation of the toluene. The resultant morphologies depend on the respective host matrix; different polymeric matrices lead to distinct *p*Na nanostructures.

In figure 2 several differences are visible between the thin films. The PS matrix leads to a considerable number of forms with relatively large elongated sizes the majority of which have at least one sharp edge. By contrast, PCL, with a tendency to form a semi-crystalline matrix, leads a small number of elongated rectangular shaped *p*Na structures with relatively sharp edges. The *p*Na structures obtained in PMMA matrices vary with the PMMA mean molecular weight. For low molecular weight PMMA, conical and needle-like forms arise, whereas medium molecular weight PMMA leads to layered *p*Na films with a mixture of sharp and jagged edges.

3. Experimental characterization

AFM Measurements

AFM imaging was performed under ambient conditions in air with a Nanosurf FlexAFM (Paralab SA, Portugal) instrument with a 100×100 μm^2 head. The measurements were carried out in tapping mode employing a Tap190Al-G from BudgetSensors, with a resonance frequency ~190 kHz and a force constant of 48 N/m.

The AFM images in figure 3 show evidence of a compact packing of the self-assembled *p*Na films that depends on the polymer host. Films grown in the presence of long chain polymeric matrices tend to have sharp-edges, sometimes assuming a layered structure, with smooth planar surfaces on the order of a micron in height. There are no noticeable ruptures, folds or fissures. On the other hand, films grown in the presence of small chain polymeric matrices give rise to textured granular surfaces, ordered in conical shapes and needles with no apparent order or growth orientation.

Wide-angle X-ray scattering

Taking advantage of the micro-focus wide-angle x-ray scattering beam line (MiNaXS)[27] at PETRA III at DESY in Hamburg, Germany the crystallographic orientation of the *p*Na thin films were investigated. The micro beam with a 13.43 keV of energy at the P03 end station, focused down to a size of 1×1μm was employed. The corresponding X-Ray diffraction patterns were recorded using a Pilatus 1K detector system with a pixel size of 172 μm and are displayed in figure 4. As might be expected from the above polarizing microscope images, the micro focused X-Ray scattering measurements reveal that the *p*Na films grown in PMMA with low molecular weight do not have a preferential crystal orientation. However, the thin films obtained in the host matrices of PS, PMMA (medium molecular weight) and PCL produce fewer peaks, raising the possibility of preferential orientation of the pNa crystals. The strongest peak observed for the *p*Na crystals grown in the presence of PS has Miller indices of [1 1 -1] with weaker peaks at [0 1 1] and [1 1 1]. PMMA medium molecular weight polymers encouraged growth that gave rise to an intense peak with Miller indices of [4 0 4], while the PCL matrix produced a film with the strongest reflection indexed as [1 3 0] and a much weaker [2 1 -4] reflection , see Table 1. In contrast, the films obtained using the PMMA matrix with lower molecular weight produced a number of diffraction peaks indicating the presence of multiple orientations. This is consistent with the AFM topography of its surface suggesting a random agglomeration of *p*Na nanocrystals. We note that for all of our samples it is very likely

that several prominent lower angle diffraction peaks are obscured by the strong background diffraction rings produced by the polymer and glass supports.

Table 1 – Identified x-ray diffraction angles of the *p*Na crystals in the respective polymeric matrices and the respective theoretical values based on the structure of [28].

Structure	Miller Indices	Observed 2θ (degrees)	Theoretical 2θ (degrees)
*p*Na/PS	[011]	10.69	10.68
	[11-1]	11.45	11.44
	[111]	11.53	11.56
*p*NA/PMMA	[404]	30.67	30.70
*p*Na/PCL	[130]	26.63	26.69
	[21-4]	27.47	27.54

Raman analyses

A high-resolution Raman spectrometer, Horiba LabRAM HR Evolution confocal microscope using a laser excitation at 532 nm (2.33 eV), was employed to characterize the bulk molecular order and orientation of the *p*Na in all the different thin films. A 100x objective lens was used to focus the laser onto the sample. Polarized Raman spectra were obtained at room temperature between 600-1800cm^{-1} corresponding to the internal molecular vibrations. The Raman spectrum of *p*Na is sensitive to its physical phase state[29–31]. The most salient feature of crystalline *p*Na's Raman spectra is a broad intense peak at 1282 cm^{-1}. In figure 5, the Raman bands of the films displayed in figure 2b) and 2c) present three prominent lines at 862 cm^{-1}, 1282 cm^{-1} and 1316 cm^{-1} all of which can be assigned to the Raman spectrum of *p*Na in its crystalline form. On the other hand, the Raman bands of the films displayed in 2a) and 2d) are dominated by two lines at 862 cm^{-1} and 1276 cm^{-1} with a substantial red shift ($\approx$ 6 cm^{-1}) in relation to the other films and the bulk crystalline form. The most striking feature of figure 5 is the absence of the Raman band cantered at 1316 cm^{-1} and a red shift of $\approx$ 6 cm^{-1} and a broadening of $\approx$ 5 cm^{-1} in the band 1282 cm^{-1} in the spectra corresponding to films grown in PS and PCL hosts.

The peaks centered at 1282 cm^{-1} is attributed to a Fermi resonance between a symmetric benzene ring vibrations and a combination line from a lower frequency symmetric ring vibration and the torsion motion of the amine group [31]. The strength of this resonance is sensitive to the localization of the π electrons. In the crystalline state, strong hydrogen bonding promotes an

increase of the electron density around the C-N bonds with the amine and nitro groups, leading to a pseudo-quinoidal configuration enhancing the intensity of the ω_3 Raman band. In contrast in non-polar liquids, the π electron cloud assumes a largely aromatic distribution and the Raman peak near 1280 cm^{-1} is reduced in intensity. Harrand has shown [31] that for crystalline *p*Na this intense band shifts and narrows with increasing temperature moving from 1276.8 cm^{-1} at 30 K to 1284.4 cm^{-1} at 300 K, reflecting a blue shift with an increase in the intermolecular distances. This suggests that the red shift of the 1280 cm^{-1} band observed for the *p*Na/PS and *p*Na/PCL systems might be associated with smaller intermolecular distances and consequently slightly stronger hydrogen bonding.

The Raman line near 1316 cm^{-1} was assigned by Harrand [31] to a bending motion of the CH groups, while that at approximately 865 cm^{-1} is associated with a bending mode of the nitro group. Both of these bands are less intense relative to the main 1282 cm^{-1} line in the *p*Na/PS and *p*Na/PCL films, while the lower weight PMMA enhances their relative intensity. We suspect that the relative decrease in the 1282cm^{-1} line observed in the low weight PMMA system indicates a more random orientation of the *p*Na nanocrystals reducing the projection of the mode onto the incident laser polarization. We note that this film generates very little if any second harmonic light and produces the weakest Raman signal overall. In contrast, the *p*Na/PS and *p*Na/PCL films have the strongest Raman response. The Raman bands of the medium weight PMMA thin film, (that of figure 2c) represent an intermediate arrangement. There is no shift in the 1282 cm^{-1} peak, but the peak at 1316 cm^{-1} is reduced in intensity as is the NO_2 bending mode at 865 cm^{-1}. This might reflect the better orientational order of the *p*Na grown in the presence of medium weight PMMA.

Polarimetry measurements

The SHG response of the *p*Na films was analysed as a function of the polarization direction of the incident light using the set-up illustrated in figure 6. The incident fundamental light (at frequency ω) is provided by a femtosecond Ti:Sapphire mode-locked laser (Coherent Mira 900F) pumped by a frequency doubled CW Neodymium-laser (Coherent Verdi 5W). The incident light had a 100 femtosecond (fs) temporal pulse width and a central wavelength of 800nm. The measurement consists in illuminating the *p*Na films with different polarization orientations and collecting and analysing the transmitted SHG field. An achromatic half-wave plate ($\lambda/2$) is placed before a 10× microscope objective with a numeric aperture (NA=0.25), in order to continuously vary the polarization direction of the incident light (0 – 360°). The SHG field is collected through a microscope objective 100× Mitutoyo Plan infinity-corrected long working distance objective (NA=0.7). A set of filters are used to reduce the incident beam

intensity and select the SHG field with a central frequency of 2ω. Before detection the generated second harmonic light is analysed using a linear polarizer, fixed to be either parallel to the incident polarization that gave rise to the highest SHG signal (q-p configuration) or perpendicular to this polarization (q-s configuration) to the incident beam polarization that produced the largest SHG signal. The analysed SHG field is recorded by focusing the beam into an optical fiber bundle connected to the entrance of a 0.3meter imaging spectrograph (Andor Shamrock SR-303i), with 0.20 nm resolution (see figure 6).

The polarimetry study of the different *p*Na films are shown in figure 7. The strongest responses are obtained for the *p*Na films grown in PS and medium weight PMMA. For these films the energy per incident pulse was approximately 17 pJ corresponding to a peak power of order 200 W. The film grown with the PCL host required a higher incident energy of roughly 660 pJ, nearly 40 times greater.

Except for the *p*Na/PCL film, the SHG polarization dependence is dominated by a cosine squared type variation indicating the dominance of a single nonlinear dipolar response orientated in the thin film plane. Consequently, *p*Na thin films grown in PS and medium weight PMMA create nonlinear mediums where the SHG signal is dominated by a single element of the second order susceptibility tensor. However, since the growth orientation are different between them, the respective tensor element corresponds to a distinct plane in each film. The clover leaf pattern of the signal from the sample grown in the presence of PCL is indicative of a cross-polarization dependence, typical of the situation when two elements of the second order susceptibility tensor, related by symmetry, have equal magnitudes. The pattern is similar to one that would be generated by a crystal with $\bar{4}2m$ symmetry such as potassium diphosphate (KDP).

Second order response estimates

To calibrate our SHG polarimetry system we replaced the *p*Na thin film samples by a 1 mm thick beta barium borate (BBO) crystal. For these measurements, the incident fundamental light consisted of pulses with an approximate energy of 4 pJ, a FWHM duration of 100 fs and a $1/e^2$ diameter of 6 mm. Using a x10 microscope objective with a numerical aperture of 0.25 to focus the fundamental beam onto the BBO crystal, we estimate that the focused fundamental beam diameter was $2\omega_0 = 2.2\ \mu m$ within the crystal. Under this tight focusing, it is necessary to take into account spatial walk-off of the second harmonic beam due to birefringence. Wang and Weiner have developed a theoretical expression taking into account both spatial walk-off and the temporal walk-off effects due to group velocity mismatch between the fundamental and second harmonic beams [32]. Assuming an incident beam with Gaussian transverse spatial and

temporal profiles, their asymptotic expression for the second harmonic generation conversion efficiency is given by,

$$\eta_{2\omega}^{BBO} = \frac{U_{2\omega}^{BBO}}{U_{\omega}^{BBO}} = \sqrt{2\ln(2)}\,\frac{\gamma U_{\omega}^{BBO} l_{S-T}}{t_p}\tan^{-1}(\mu) \qquad 1$$

Here U_ω and $U_{2\omega}$ are the energies of the incident fundamental and generated second harmonic pulses, t_p is the FWHM pulse duration of the fundamental beam, while μ is the ratio of the crystal thickness L to the incident beam's confocal length. In our situation $\mu \simeq 63$ indicating very tight focusing, allowing us to replace $\tan^{-1}(\mu)$ by its limiting value of $\pi/2$. The parameter l_{S-T} represents an effective length over which the fundamental and second harmonic beams propagate together. It is given by summing in quadrature the spatial and temporal effects according to the expression

$$l_{S-T} = \left[\left(\frac{\rho}{\omega_0}\right)^2 + 2\ln(2)\left(\frac{\beta}{t_p}\right)^2\right]^{-1/2} \qquad 2$$

where ρ denotes the angle between the ordinary and extraordinary ray's pointing vectors and β is the group velocity mismatch between the fundamental and second harmonic beams with values of $68\,mrads$ and $194\,fs/mm$ respectively for SHG of 800nm in BBO by type I phase matching. We estimate that $l_{S-T} \approx 16\,\mu m$ and is dominated by the spatial walk-off. Finally, γ represents a scaled nonlinear coupling coefficient and is given by,

$$\gamma = \frac{4\omega^2 {d_{eff}}^2}{n_\omega n_{2\omega}\lambda_0 c^3 \varepsilon_0} \qquad 3$$

with $d_{eff} = 2.0\ pm/V$ the effective second order nonlinear coefficient for SHG via type I phase matching of 800nm light with a BBO crystal, n_ω and $n_{2\omega}$ are the respective refractive indices of the two beams (both are equal to 1.660) and $\lambda_0 = 800\,nm$, giving $\gamma \approx 1.7\times10^{-2}\ s/Jm$. Substituting these values into equation (1) we estimate the second harmonic efficiency of our system to be $\eta \approx 2x10^{-4}$ well into the non-depletion regime.

Momentarily, let us assume that the observed SHG generated by the *p*Na films arises from the symmetry breaking at the surfaces. The SHG power generated by the surfaces can be described in terms of an effective surface susceptibility using the approach of Brevet[33]. According to his theoretical development, the SHG efficiency arising from a single *p*Na crystalline surface would be given by the following expression,

$$\eta_{2\omega}^{pNa} = \sqrt{\frac{2\ln 2}{\pi}} \frac{4\omega^2 \left[\chi^{(2s)}\right]^2}{n_\omega n_{2\omega} \lambda_0 c^3 \varepsilon_0} \frac{U_\omega^{pNa}}{b t_p} \quad 4$$

Here, $\left(\chi^{(2s)}\right)$ is the effective quadratic surface polarization, while b is the confocal length of the incident fundamental beam (in air) and is approximately equal to 550 μm. Small correction factors related to the Fresnel reflection and transmission coefficients have been ignored in equation 4. Combining the above expressions, we can readily obtain an estimate for the quadratic surface susceptibility of the *p*Na films,

$$\chi_{pNa}^{(2s)} = d_{eff}^{BBO} \frac{U_\omega^{BBO}}{U_\omega^{pNa}} \sqrt{\left(\frac{S_{2\omega}^{pNa}}{S_{2\omega}^{BBO}}\right)\left(\frac{\sqrt{\pi^3}}{2} l_{S-T} b\right)} \quad 5$$

where $S_{2\omega}^{(BBO,pNa)}$ is the second harmonic signal measured for the BBO crystal or *p*Na/polymeric thin film and is proportional to the energies of the respective second harmonic pulses. We have ignored small factors related to differences in the refractive indices of the BBO crystal and the *p*Na thin films. The respective estimates are reported in Table 2.

Table 2 - Estimates for the effective quadratic surface susceptibility and effective material quadratic susceptibility of the *p*Na/polymeric thin films

Material	Thickness, L (μm)	Incident pulse energy, U_ω (pJ)	SHG $S_{2\omega}$ (au)	$\chi^{(2s)}$ (nm^2/V)	d_{eff}^{pNa} (pm/V)
BBO	$1.0x10^3$	4	$1.11x10^8$	_	2.0
*p*Na/PS	1.9	17	$1.78x10^5$	2.9	1.5
*p*NA/PMMA (Spot 1)	2.7	17	$7.06x10^5$	5.8	2.1
*p*NA/PMMA (Spot 2)	2.0	17	$9.52x10^5$	6.7	3.3
*p*Na/PCL	0.9	660	$3.23x10^4$	0.03	0.03

Alternatively, if the second harmonic light is generated throughout the thickness of the thin pNa crystal one can use the standard plane wave result for estimating the effective quadratic susceptibility coefficient, d_{eff}^{pNa} ,

$$\eta_{2\omega}^{pNa} = \frac{4\omega^2 \left[d_{eff}^{pNa}\right]^2}{n_\omega n_{2\omega} \lambda_0 c^3 \varepsilon_0} \sqrt{\frac{2\ln 2}{\pi}} \frac{U_\omega^{pNa} L_{pNa}^2}{b t_p} \quad 6$$

Since the propagation of the fundamental light within the thin films is on the order of a few wavelengths phase mismatch between the fundamental and second harmonic waves can be safely ignored. In addition, neither temporal separation nor spatial separation, due to group velocity mismatch and birefringence respectively, are relevant. Combining this relation with equation 1 we arrive at the following estimate for the effective quadratic susceptibility of the *p*Na thin films,

$$d_{eff}^{pNa} = d_{eff}^{BBO} \frac{U_{\omega}^{BBO}}{U_{\omega}^{pNa}} \sqrt{\left(\frac{S_{2\omega}^{pNa}}{S_{2\omega}^{BBO}}\right)\left(\frac{\sqrt{\pi^3} l_{S-T} b}{2L_{pNa}^2}\right)} \qquad 7$$

Again we have ignored small corrections that take into account the difference in the refractive indices of the nonlinear media. The above relation is used to estimate the last column of values in Table 2.

Using equation 5 the $\chi^{(2s)}$ for the *p*Na films grown with PS (figure 2a) is roughly $\chi^{(2s)} \simeq 3\,\mathrm{nm}^2/\mathrm{V}$, roughly a factor of twenty below that estimated for *p*Na nanocrystals assembled inside of PMMA polymeric electrospun nanofibers [4]. For the *p*Na crystals grown with medium weight PMMA the values obtained are factors of 2 and 2.3 greater for the two different spots measured (se figure 2c). Finally, the signal from the *p*Na/PCL films of figure 2d) leads to an estimate which is roughly a factor of 100 lower than the *p*Na/PS sample. We note however that these estimates are for a single surface, whereas it is quite likely the eletrospun fibers contain multiple *p*Na nanocrystals within the area illuminated by the incident fundamental beam. In comparison, the quadratic surface susceptibility values estimated theoretically by Malagoli and Munn [34] for an isolated surface of a bulk *p*Na crystal are three orders of magnitude lower than the above estimates for the *p*Na medium weight PMMA system. The highest surface quadratic susceptibility tensor element they estimate is $\chi_{zzz}^{(2s)} = -1.416\times10^{-3}\,\mathrm{nm}^2/\mathrm{V}$ for a surface with Miller indices of (004). This implies that the large second order nonlinear response of these systems must be due to an interaction with the underlying polymeric matrix.

On the other hand, it is plausible that interactions at the polymer/*p*Na crystals surface leads to slight strains or distortions that break the nominal centrosymmetry of the *p*Na crystals over a distance extending more than a few atomic layers into the crystal. However, given that the thicker *p*Na/PMMA sample produced a slightly lower signal, this symmetry breaking appears not to extend throughout the full sample thickness. Nevertheless, the estimates in the last column provide an interesting basis for comparison with previous studies. Hwang et al. [35] obtained strong second harmonic generation from *p*Na /PS mixtures that were formed by flash

evaporation from a toluene solution. When the *p*Na concentration was 10% by weight they observed a signal over 1000 times greater than urea which has a nonlinear coefficient of $d_{36} \simeq 1.2 pm/V$ [36]. Earlier in 1988 Miyazaki et al. [24] observed SHG from a cast benzene solution of a *p*Na/ PCL (Mw = 75000) composite that that was 115 times as large as urea when the *p*Na composition was 20% by weight. Although our observations lead to lower effective second order nonlinear coefficients, we note that the previous systems investigated by Hwang et al. and Miyazaki et al. are both highly scattering, whereas our *p*Na/ polymeric films have fair optical quality (as seen by the images of figure 2), an advantage for many potential applications. Furthermore, the x-ray data suggest that our films are preferentially oriented crystals, so that it might be possible to improve the SHG response by optimizing the fundamental beam's angle of incidence.

In summary, except for the low weight PMMA-*p*Na films, all of the samples produce second harmonic light with good efficiency observable by the naked eye with low energy fundamental pulses. The above estimated quadratic surface susceptibilities are all several orders of magnitude greater than that expected from an isolated *p*Na crystalline surface based on the estimates of Malagoli and Munn [34]. We note that these authors predict that the dominant contribution from the centrosymmetry breaking at the crystal surface rapidly vanish. The dominant contributions come from the first two unit cells. We hypothesize that interactions with the polymeric hosts, most likely through hydrogen bonding, introduces alteration of the normally centrosymmetric head to tail crystalline structure of *p*Na that persists over multiple molecular layers enhancing the second harmonic response relative to that of an isolated crystal.

4. Conclusion

In this study, we have shown it is possible to obtain a strong macroscopic second harmonic response from *p*Na molecules organized in a layered thin film with good optical quality. A modified version of capillary growth was used to obtain various *p*Na thin films in different host polymeric matrices. The thin films here obtained in a confined environment have distinct nonlinear optical properties compared to bulk *p*Na crystals. It was observed that matrix with long molecular chains tend to produce lamellar structures which favour SHG while matrices with short molecular chains leads to randomly oriented *p*Na microstructures that do not generate appreciable second harmonic light. The strength of the observed SHG signal in these systems, is roughly an equivalent to that previously measured in electro- spun *p*Na-PMMA fibers [4], if one assumes that any given ray of the incident fundamental beam will encounter on average 3-5 *p*Na nanocrystals when traversing the fibers. This suggests that rather than the strong dc electric fields applied during the electro-spinning process, *p*Na-polymer interactions

are likely to play a major role in inducing the strong SHG response. Future efforts will explore whether the response of these films can be optimized by varying the relative *p*Na – polymer concentration or by changing the temperature under which the films are formed.

The fabrication method used here should be extendable to other organic molecules with large dipole moments and strong second order nonlinear optical responses that crystalize primarily though hydrogen bonding via the donor and acceptor moieties. Given the large number of NLO active organic compounds that crystallize in centrosymmetric crystalline structures; this technique has the potential to open up a new pathway to fabricate sub-wavelength photonic materials into with large second order nonlinear optical responses. The thin films here obtained in a confined environment have distinct optical nonlinear properties in relation to that of the ordered bulk structure.

5. Acknowledgements

Hugo Gonçalves thanks the Portuguese Foundation for Science and Technology (FCT) for the support under grant PD/BD/111873/2015. The equipment used to characterize the second harmonic response of the thin films was acquired within the framework of the Portuguese National Program for Scientific Re-equipment, contract REEQ-25/FIS/2005 with funds from POCI 2010 (FEDER) and FCT. The Raman microscope was acquired through the project nSTeP Nanostructured Systems for Tailored Performance, NORTE-07-0124-FEDER-000039, ON.2. The authors thank Desy at PETRA P03, Hamburg Germany for beam time and support through the project I-20170586 EC.

References

[1] Cabanetos C, Bentoumi W, Silvestre V, Blart E, Pellegrin Y, Montembault V, Barsella A, Dorkenoo K, Bretonnière Y, Andraud C, Mager L, Fontaine L and Odobel F 2012 New cross-linkable polymers with Huisgen reaction incorporating high μβ chromophores for second-order nonlinear optical applications *Chem. Mater.* **24** 1143–57

[2] Vallée R, Damman P, Dosière M, Toussaere E and Zyss J 2000 Nonlinear optical properties and crystalline orientation of 2-methyl-4- nitroaniline layers grown on nanostructured poly(tetrafluoroethylene) substrates *J. Am. Chem. Soc.* **122** 6701–9

[3] Li M, Li Y, Zhang H, Wang S, Ao Y and Cui Z 2017 Molecular engineering of organic chromophores and polymers for enhanced bulk second-order optical nonlinearity *J. Mater. Chem. C* **5** 4111–22

[4] Goncalves H, Saavedra I, Ferreira R A S, Lopes P E, De Matos Gomes E and Belsley M 2018 Efficient second harmonic generation by para-nitroaniline embedded in electro-

spun polymeric nanofibres *J. Phys. D. Appl. Phys.* **51**

[5] Rau I, Armatys P, Chollet P A, Kajzar F and Zamboni R 2006 Conjugated polymers oriented organic thin films for nonlinear optics *Molecular Crystals and Liquid Crystals* vol 446 pp 23–45

[6] Ledoux I and Zyss J 2002 Molecular engineering of molecules and materials for quadratic nonlinear optics *Comptes Rendus Phys.* **3** 407–27

[7] Jonathan W. Steed J L A 1993 Supramolecular chemistry. *Science* **260** 1762–3

[8] Maymó M, Martorell J, Molinos-Gómez A and López-Calahorra F 2006 Visible second-harmonic light generated from a self-organized centrosymmetric lattice of nanospheres. *Opt. Express* **14** 2864–72

[9] Kajzar F, Messier J, Chemla D S and Zyss J 1987 Nonlinear Optical Properties of Organic Molecules and Crystals *by DS Chemla J. Zyss, Acad. Press. New York* **1** 51

[10] Bhattacharya S and Saha B K 2011 Inclusion of a chiral guest in a centrosymmetric organic host lattice *CrystEngComm* **13** 6941–4

[11] Zappe H 2010 Fundamentals of Micro-optics Technology , Devices and Applications

[12] Papadopoulos M G, Sadlej A J and Leszczynski J 2006 *Non-Linear Optical Properties of Matter*

[13] Werner L, Caro J and Finger G 1992 Optical second harmonic generation (SHG) on p-nitroaniline in large crystals of AlPO.hlf.4.rhlf.-5 and ZSM-5 *Zeolites* **12** 658–63

[14] Dadsetani M and Omidi A R 2015 Linear and nonlinear optical properties of 3-nitroaniline (m-NA) and 4-nitroaniline (p-NA) crystals: A DFT/TDDFT study *J. Phys. Chem. Solids* **85** 117–31

[15] Parka C, Choia U and Kimb C 1995 Theoretical Study of the Structures and Nonlinear Optical Properties of Hydrogen-Bonded Nitroaniline Systems **71** 1701–2

[16] Damman P, Vallée R, Dosière M, Toussaere E and Zyss J 2001 Oriented crystallization of NLO organic materials *Synthetic Metals* vol 124 pp 227–32

[17] Gauvin S and Zyss J 1996 Growth of organic crystalline thin films, their optical characterization and application to non-linear optics *Journal of Crystal Growth* vol 166 pp 507–27

[18] Henningsen T, Singh N B, Hopkins R H, Mazelsky R, Hopkins F K, Frazier D O and Singh O P 1994 Growth of binary organic NLO crystals: m.Na-p.NA and m.Na-CNA

systems *Mater. Lett.* **20** 203–9

[19] Lalama S J and Garito A F 1979 Origin of the nonlinear second-order optical susceptibilities of organic systems *Phys. Rev. A* **20** 1179–94

[20] Werner L, Caro J, Finger G and Kornatowski J 1992 Optical second harmonic generation (SHG) on p-nitroaniline in large cyrstals of AIPO4-5 and ZSM-5 *Zeolites* **12** 658–63

[21] Isakov D V., Belsley M S, De Matos Gomes E, Gonçalves H, Schellenberg P and Almeida B G 2014 Intense optical second harmonic generation from centrosymmetric nanocrystalline para-nitroaniline *Appl. Phys. Lett.* **104** 181903

[22] Kobayashi H and Kotani M 1996 Observation of Generation of Intense Second-Harmonics at Etch Pits of p -Nitroaniline Single Crystal Surface *Mol. Cryst. Liq. Cryst. Sci. Technol. Sect. A. Mol. Cryst. Liq. Cryst.* **278** 125–30

[23] Kobayashi H and Kotani M 1994 Study of single crystal surface with second-harmonic generation: P-nitroaniline *Mol. Cryst. Liq. Cryst. Sci. Technol. Sect. A. Mol. Cryst. Liq. Cryst.* **252** 277–81

[24] Miyazaki T, Watanabe T and Miyata S 1988 Highly efficient second harmonic generation in p-nitroaniline/poly(lactone) systems *Jpn. J. Appl. Phys.* **27** L1724–5

[25] Manetta S, Ehrensperger M, Bosshard C and Günter P 2002 Organic thin film crystal growth for nonlinear optics: Present methods and exploratory developments *Comptes Rendus Phys.* **3** 449–62

[26] Sherwood J N and Simpson G S 1993 The growth, structural and optical characterization of large area, single crystalline thin films of 3-nitroaniline (mNA) *J. Cryst. Growth* **128** 981–5

[27] Buffet A, Rothkirch A, Döhrmann R, Körstgens V, Abul Kashem M M, Perlich J, Herzog G, Schwartzkopf M, Gehrke R, Müller-Buschbaum P and Roth S V. 2012 P03, the microfocus and nanofocus X-ray scattering (MiNaXS) beamline of the PETRA III storage ring: The microfocus endstation *J. Synchrotron Radiat.* **19** 647–53

[28] Trueblood K N, Goldish E and Donohue J 1961 A three-dimensional refinement of the crystal structure of 4-nitroaniline *Acta Crystallogr.* **14** 1009–17

[29] Harrand M 1979 Raman study on p-nitroaniline: Molecular structure in the molten phase *J. Raman Spectrosc.* **8** 161–4

[30] Marlow F, Hill W, Caro J and Finger G 1993 Raman-Study on P-Nitroaniline in

Channels of the Molecular-Sieve Alpo(4)-5 *J. Raman Spectrosc.* **24** 603–8

[31] Harrand M 1975 Raman study on para nitroaniline single crystal. II: Internal Vibrations *J. Raman Spectrosc.* **4** 53–73

[32] Wang H and Weiner A M 2003 Efficiency of Short-Pulse Type-I Second-Harmonic Generation With Simultaneous Spatial Walk-Off, Temporal Walk-Off, and Pump Depletion *IEEE J. Quantum Electron.* **39** 1600–18

[33] Brevet P F 1996 Phenomenological three-layer model for surface second-harmonic generation at the interface between two centrosymmetric media *J. Chem. Soc. Faraday Trans.* **92** 4547

[34] Malagoii M and Munn R W 2000 Microscopic calculation of surface-induced second-harmonic generation in crystals of para-nitroaniline *J. Chem. Phys.* **112** 6757–62

[35] Hwang Y, Garetz B A and Okamoto Y 1992 Second-harmonic generation in pure p-nitroaniline and in composites with polystyrene by flash evaporation *Opt. Lett.* **17** 487–9

[36] Dmitriev V G, Gurzadyan D D and Nikogosyan D N 1997 *Handbook of Nonlinear Optical Crystals* (Berlin: Springer Verlag)

Figure Captions:

Figure 1 – The method used to obtain the two-dimensional *p*Na-polymeric thin films.

Figure 2 – Several representative *p*Na thin films obtained using different polymeric matrices: a) a PS matrix, b) low molecular weight PMMA, c) medium molecular weight PMMA and d) PCL matrix. The images were taken using a microscope equipped with a combination polarizer/analyser under incoherent white light illumination.

Figure 3 – AFM topography of the surface of films presented in figure 2 and the respective thicknesses. In a) PS matrix, b) low molecular weight PMMA, c) medium molecular weight PMMA and d) PCL matrix. The samples were partially destroyed during separation of the glass slides necessary to perform the measurement. The measurements were performed at the edge of the thin film structures. In the cases of the low and medium weight PMMA matrices, the specific location is marked with a red square in figure 2b and 2c.

Figure 4 – X-Ray diffractograms of the thin films presented in figure 2. The red arrow represents the **Q** vector normal to the diffracting planes. (a) *p*Na/PS matrix, (b) *p*Na/low molecular weight PMMA, (c) *p*Na/medium molecular weight PMMA and (d) *p*Na/PCL matrix.

Figure 5 – Raman spectrum of the films represented in figure 2. A red shift is observed in the peak characteristic of the crystalline state at frequency $\nu = 1284\ \mathrm{cm}^{-1}$ in the spectra of figures 2a) and 2d).

Figure 6 - Polarimetry Setup. The sample is excited by a linearly polarized Ti:Sapphire laser beam. The polarization of the incident beam is continuously varied using an achromatic half-wave wave plate (WP – λ/2). A 10x objective is used to focus the beam on the sample. The SHG is collected via a 100x objective. A set of bandpass filters are used to eliminate the fundamental beam. After passing through a fixed polarization analyser (P) the SHG signal is detected using a cooled CCD array coupled to a 0.3 m spectrograph.

Figure 7 - Polar plots of the SHG intensity of the pNa-polymer films represented in figure 2. a) displays the SHG polarimetry data of the *p*Na-PS thin film shown in figure 2a), acquired using an incident beam with an average pulse energy ≈ 17 pJ. b) and c) display the SHG polarimetry data for the pNa-medium weight PMMA films obtained at the illuminated spots 1 and 2 respectively as marked in figure 2c). The incident beam had average energy per pulse ≈ 17 pJ. d) shows the data of the *p*NA-PCL film displayed in figure 2d). In this case the SHG signal is much lower, requiring a higher average incident energy per pulse of ≈ 660 pJ.

Figure 1

Click here to download high resolution image

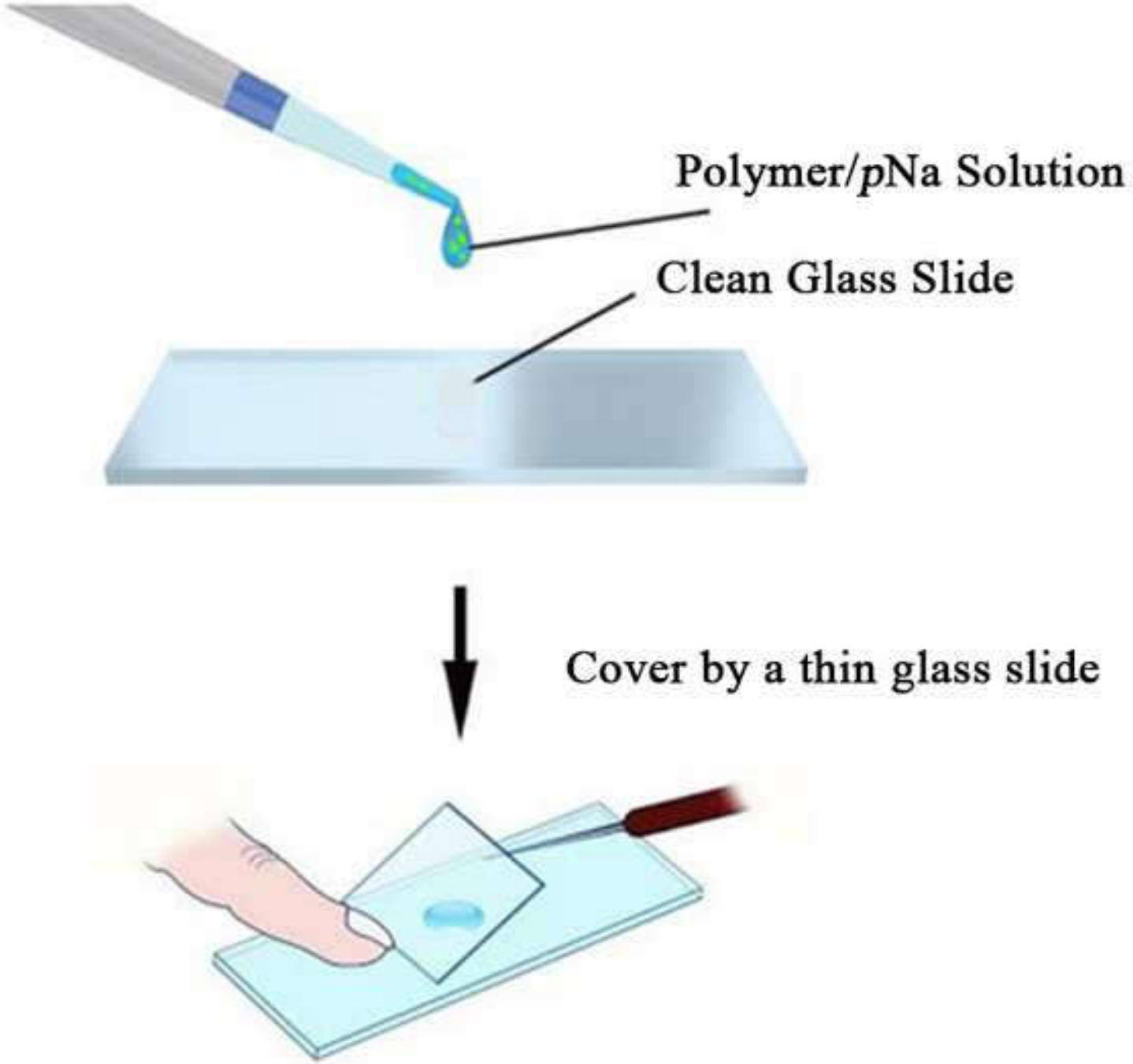

Figure 2a
Click here to download high resolution image

Figure 2b
Click here to download high resolution image

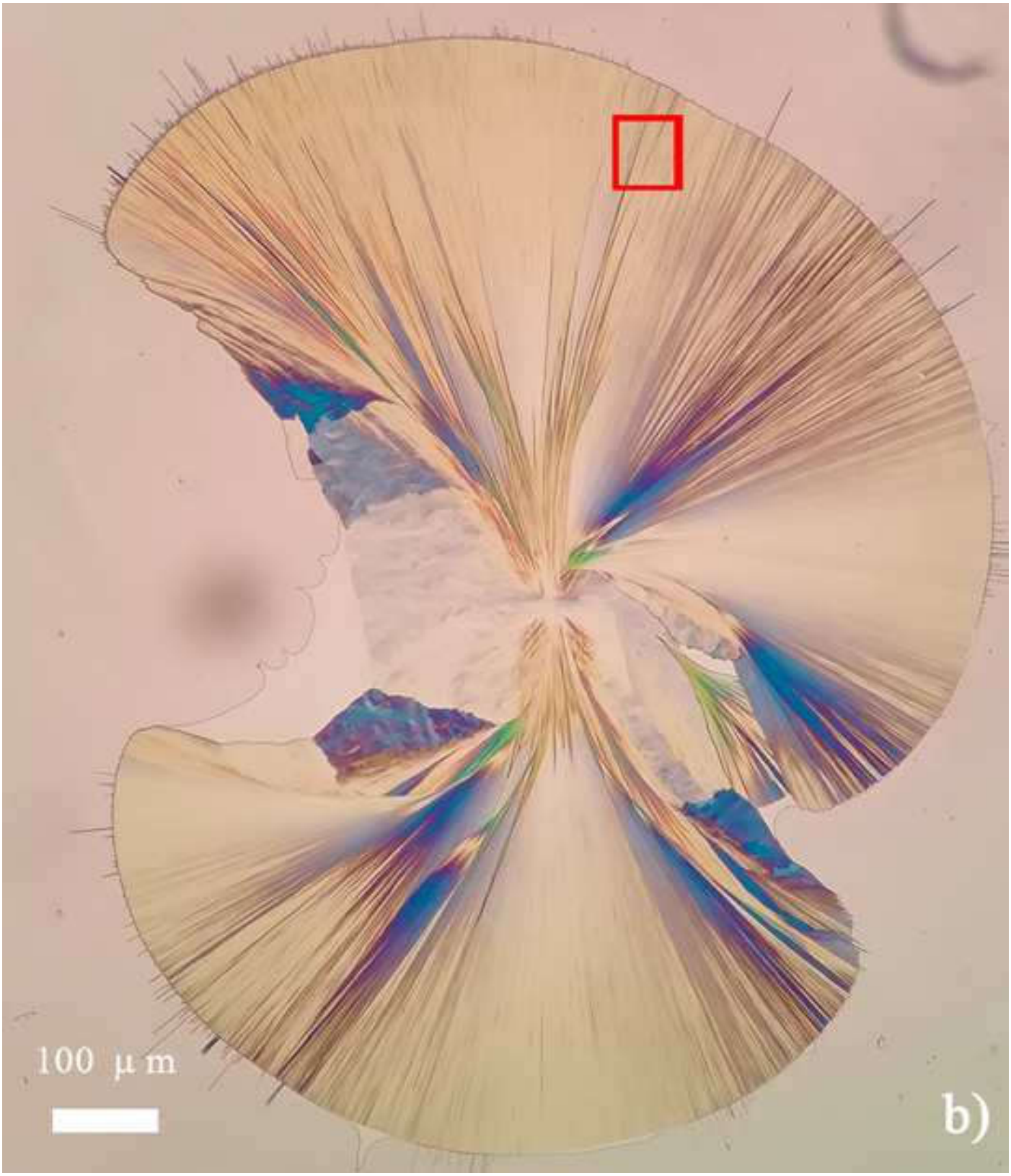

Figure 2c
Click here to download high resolution image

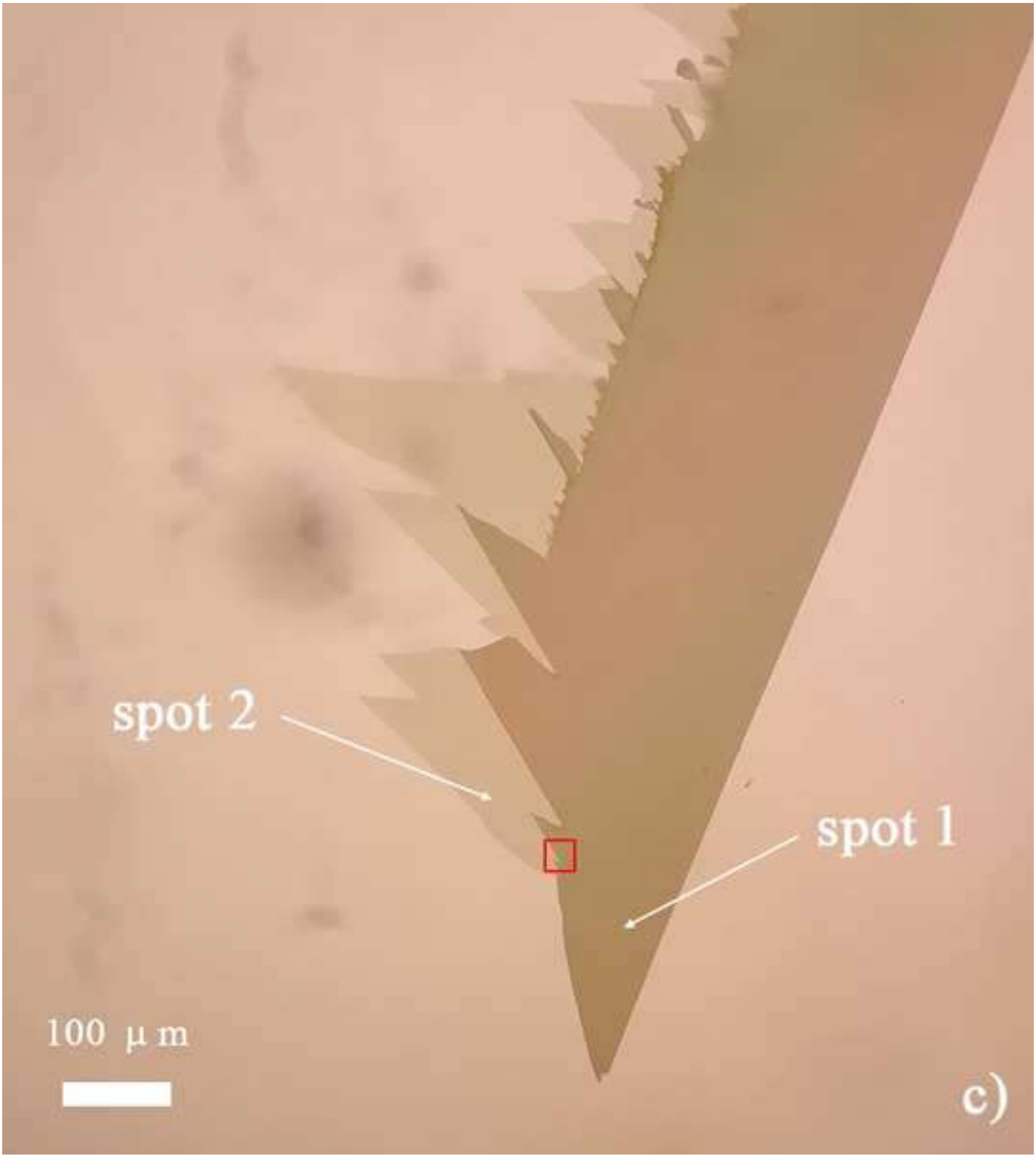

Figure 2d
Click here to download high resolution image

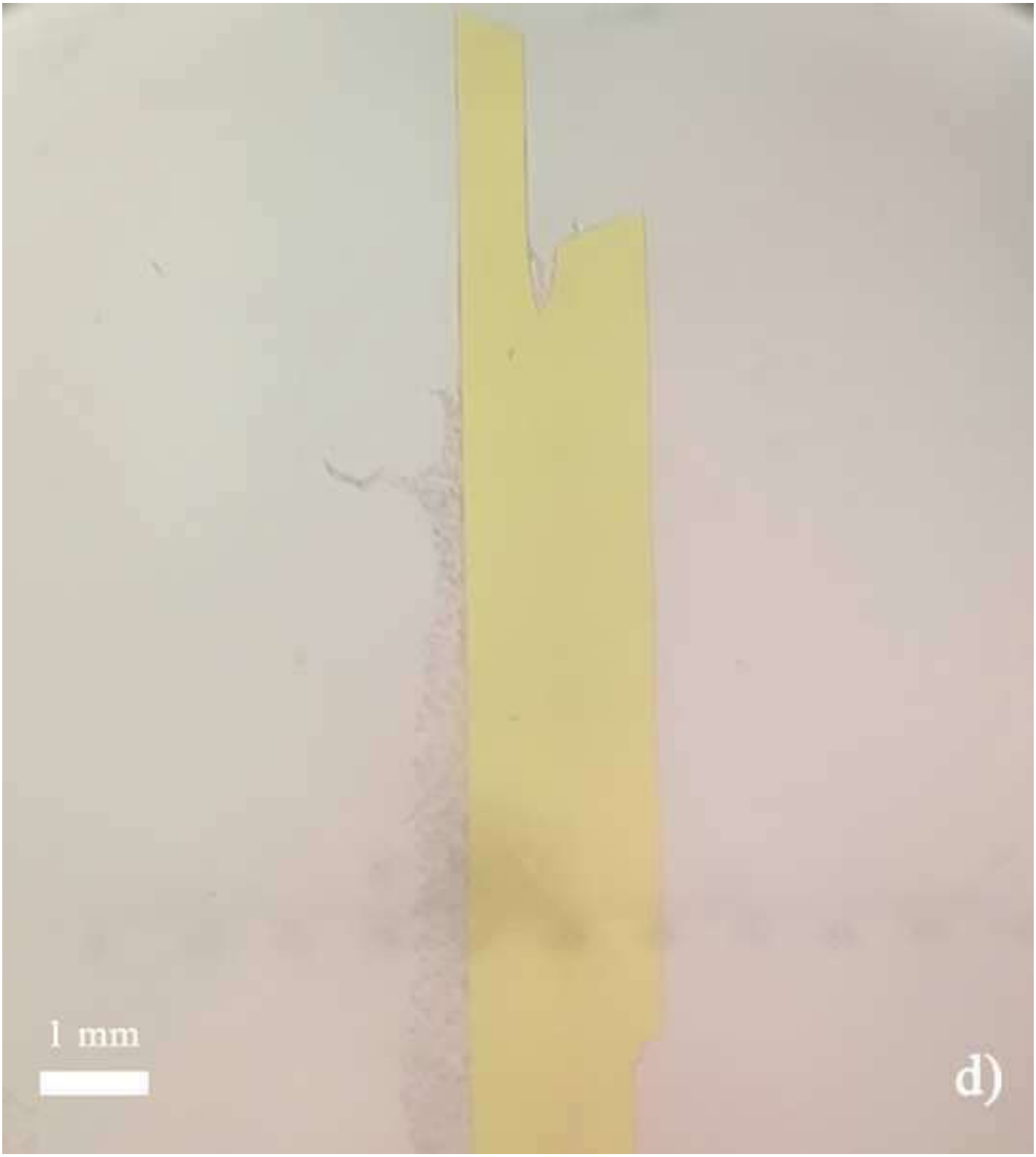

Figure 3a
Click here to download high resolution image

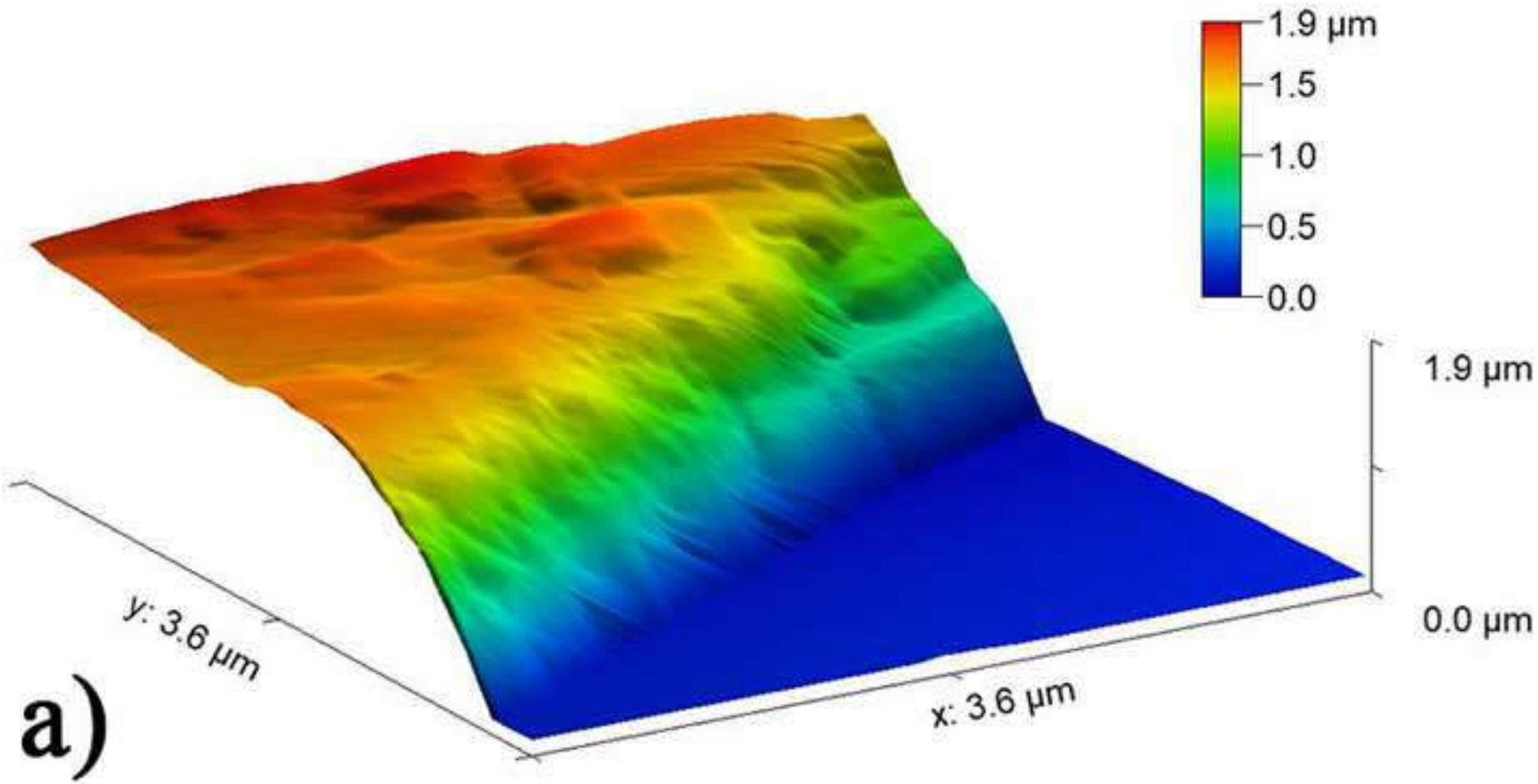

Figure 3b
Click here to download high resolution image

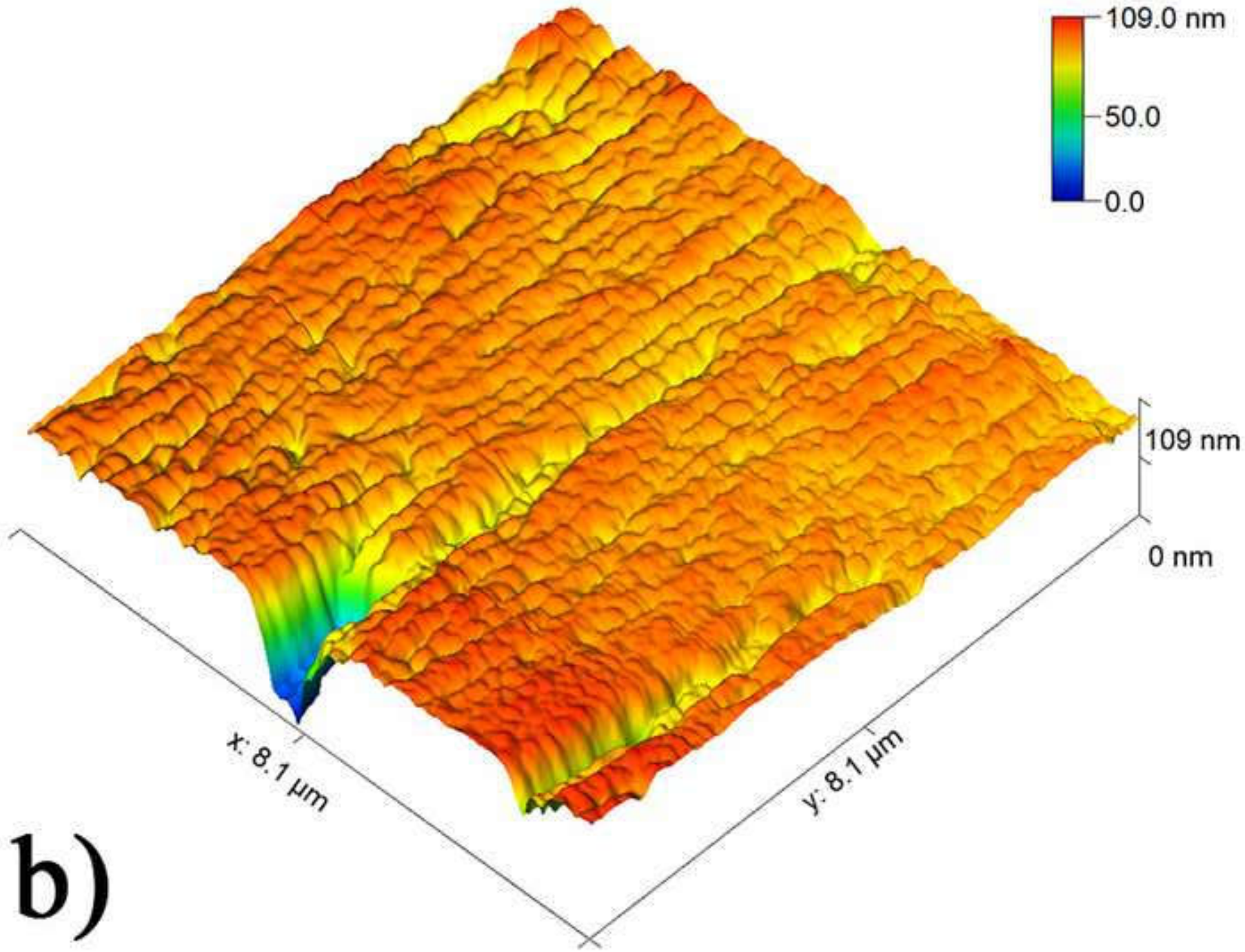

Figure 3c
Click here to download high resolution image

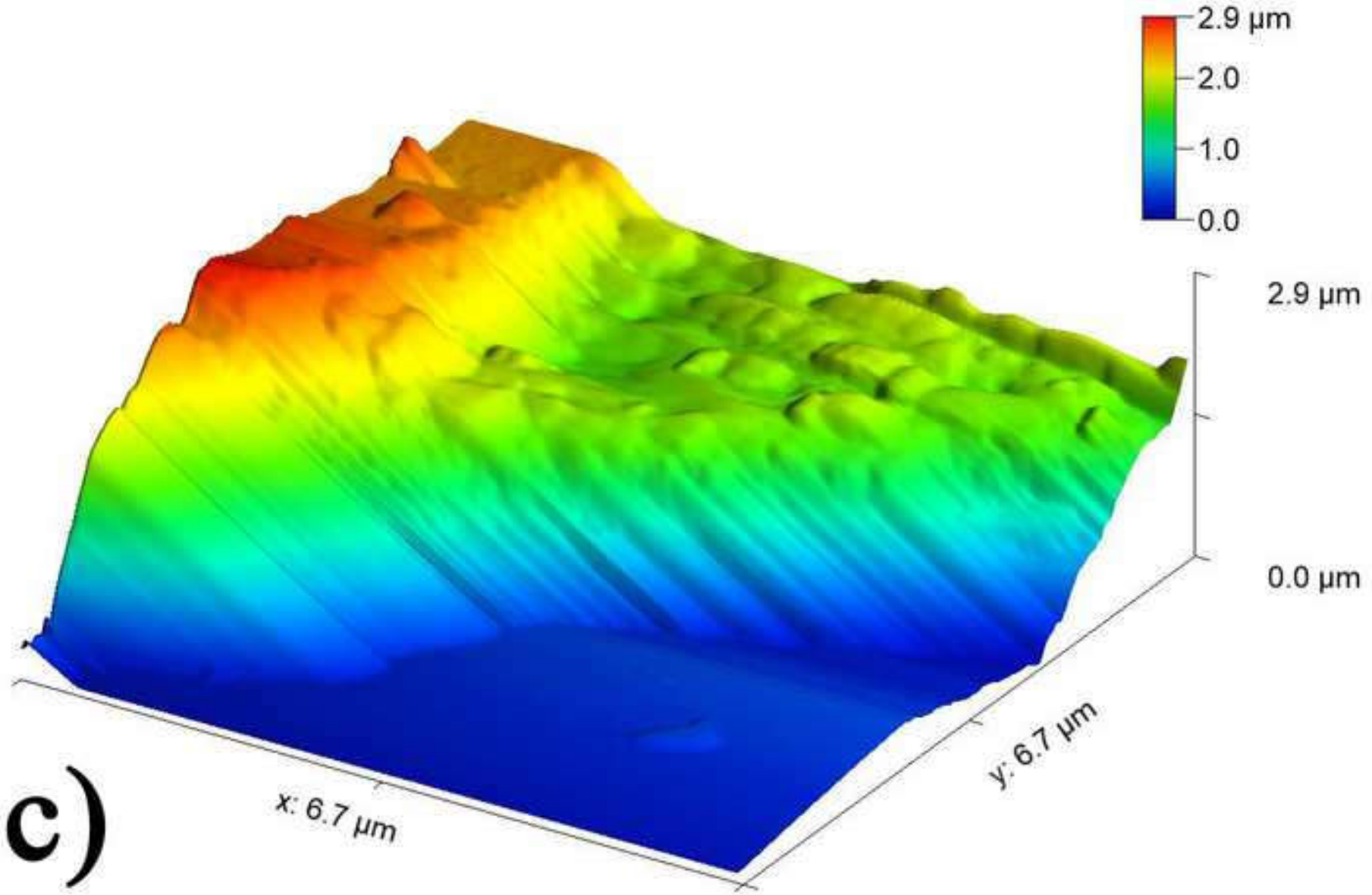

Figure 3d
Click here to download high resolution image

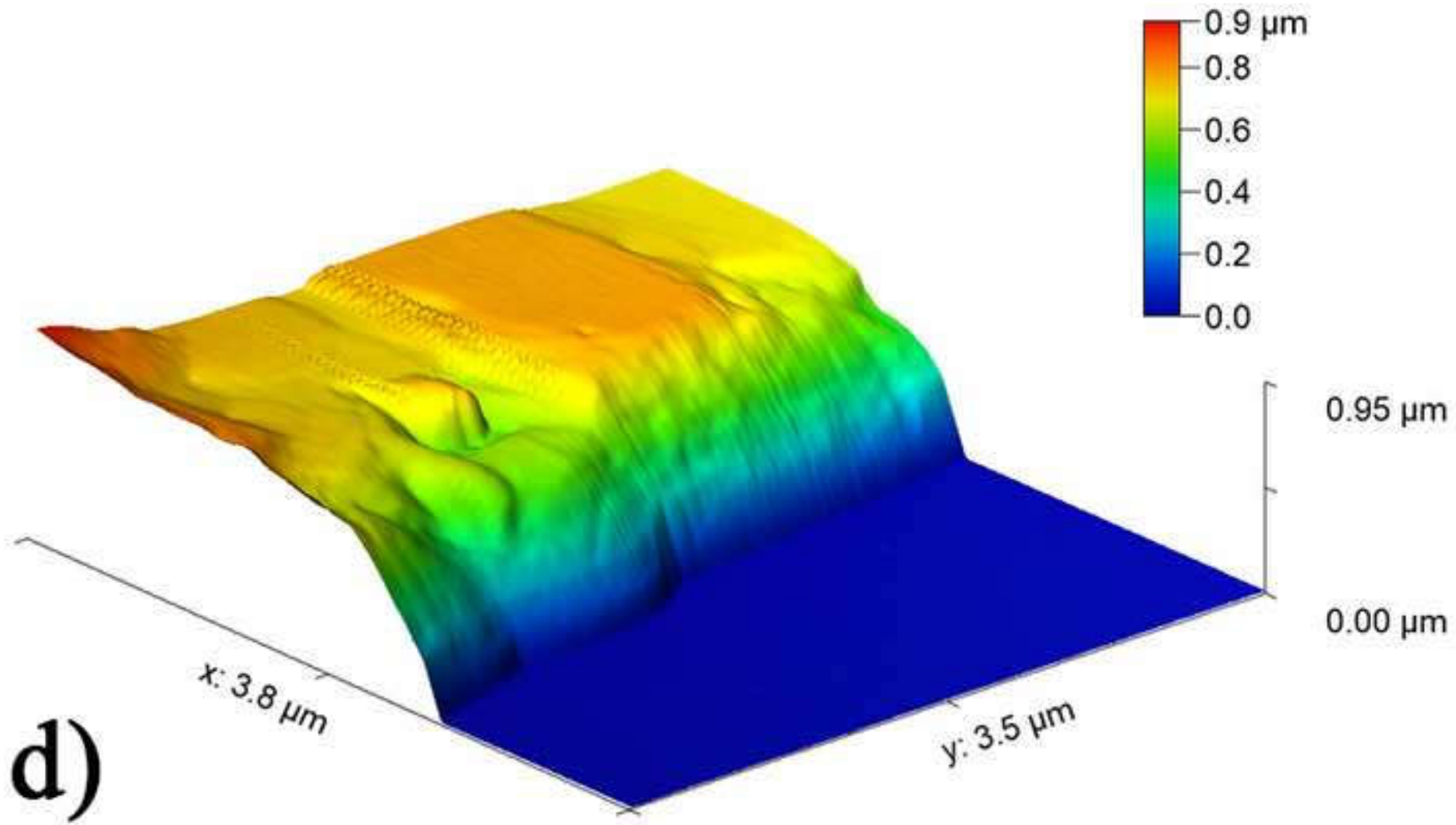

Figure 5
Click here to download high resolution image

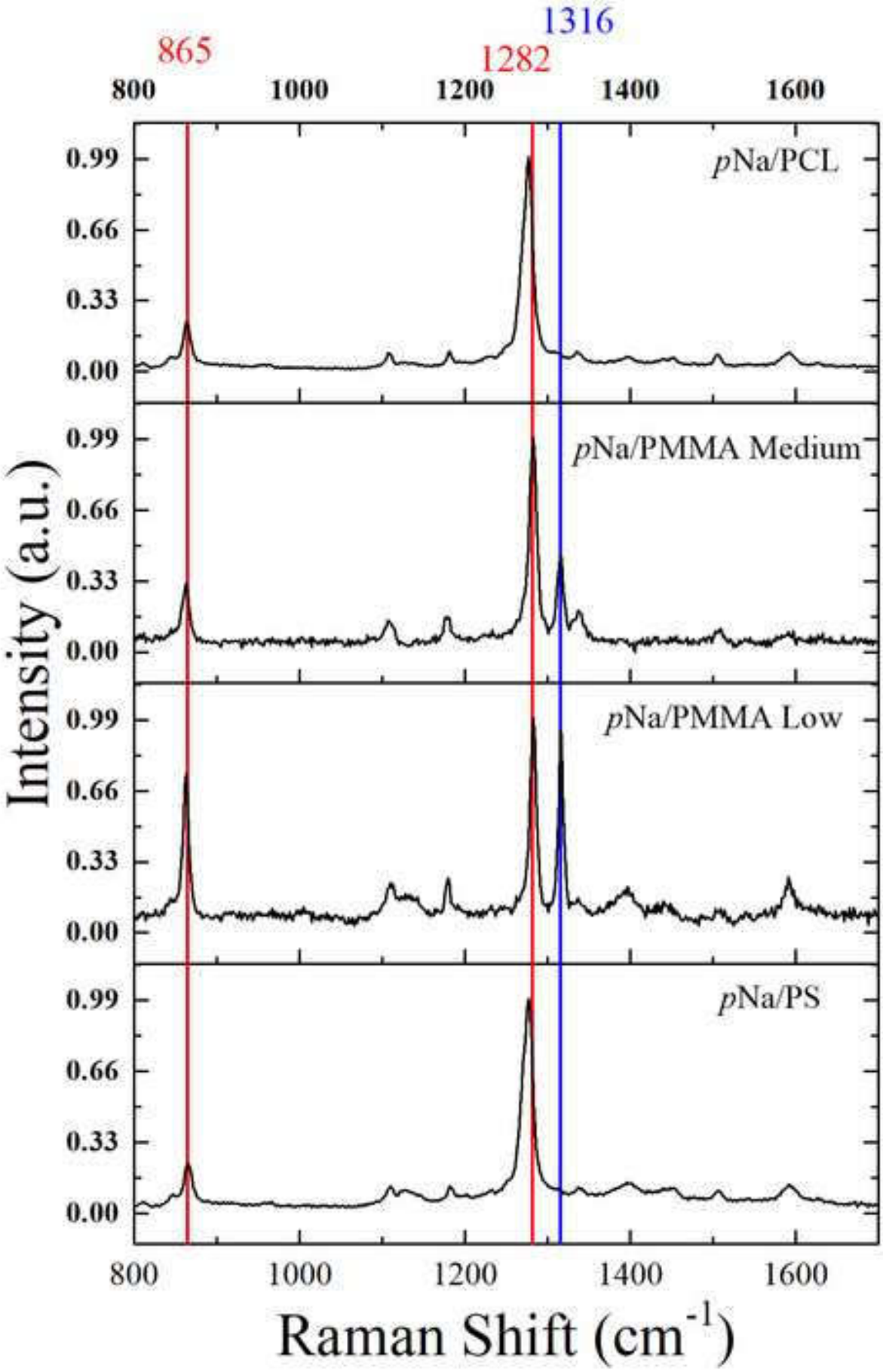

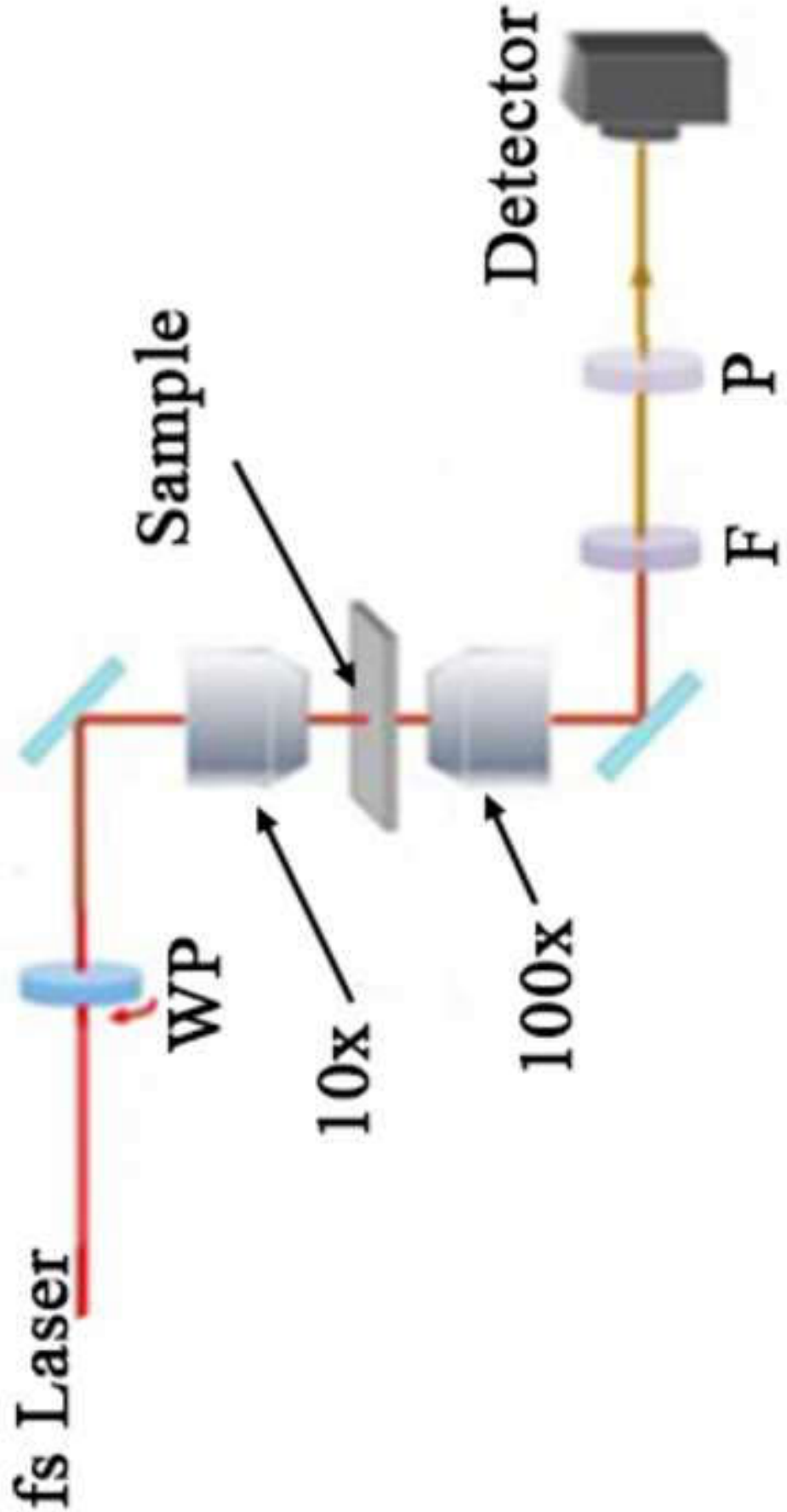

Figure 6
Click here to download high resolution image

Figure 7a
Click here to download high resolution image

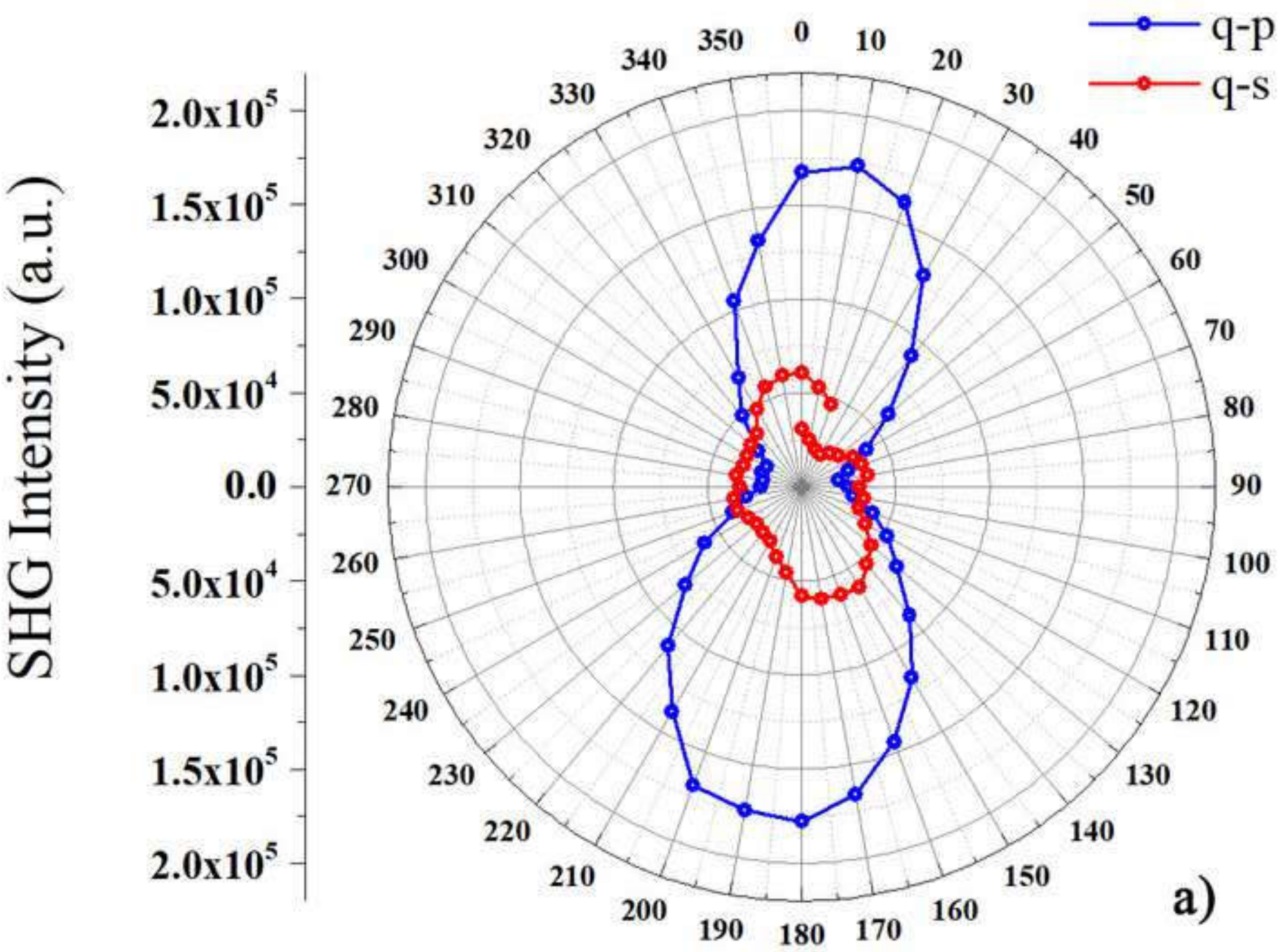

Figure 7b
Click here to download high resolution image

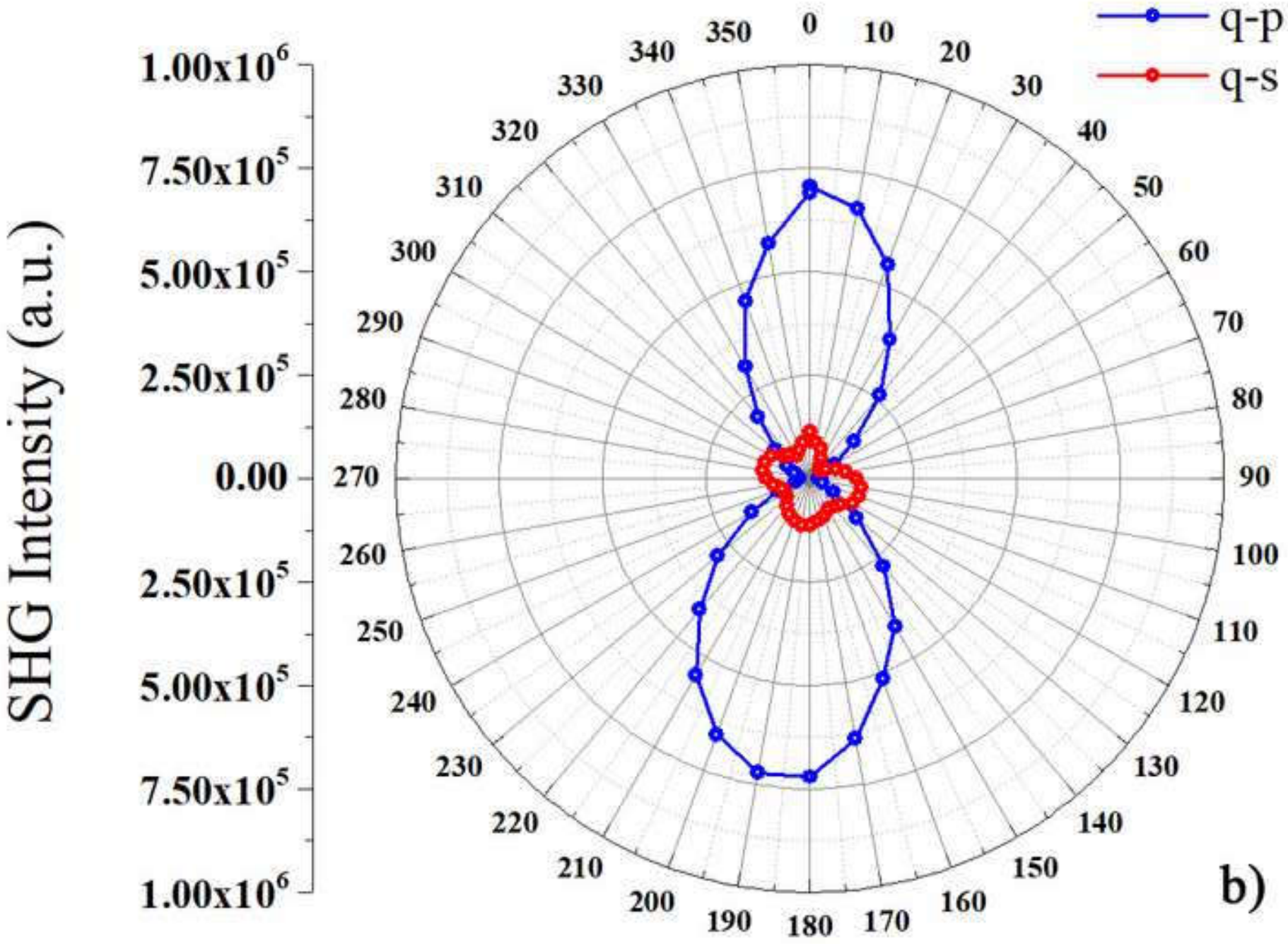

Figure 7c
Click here to download high resolution image

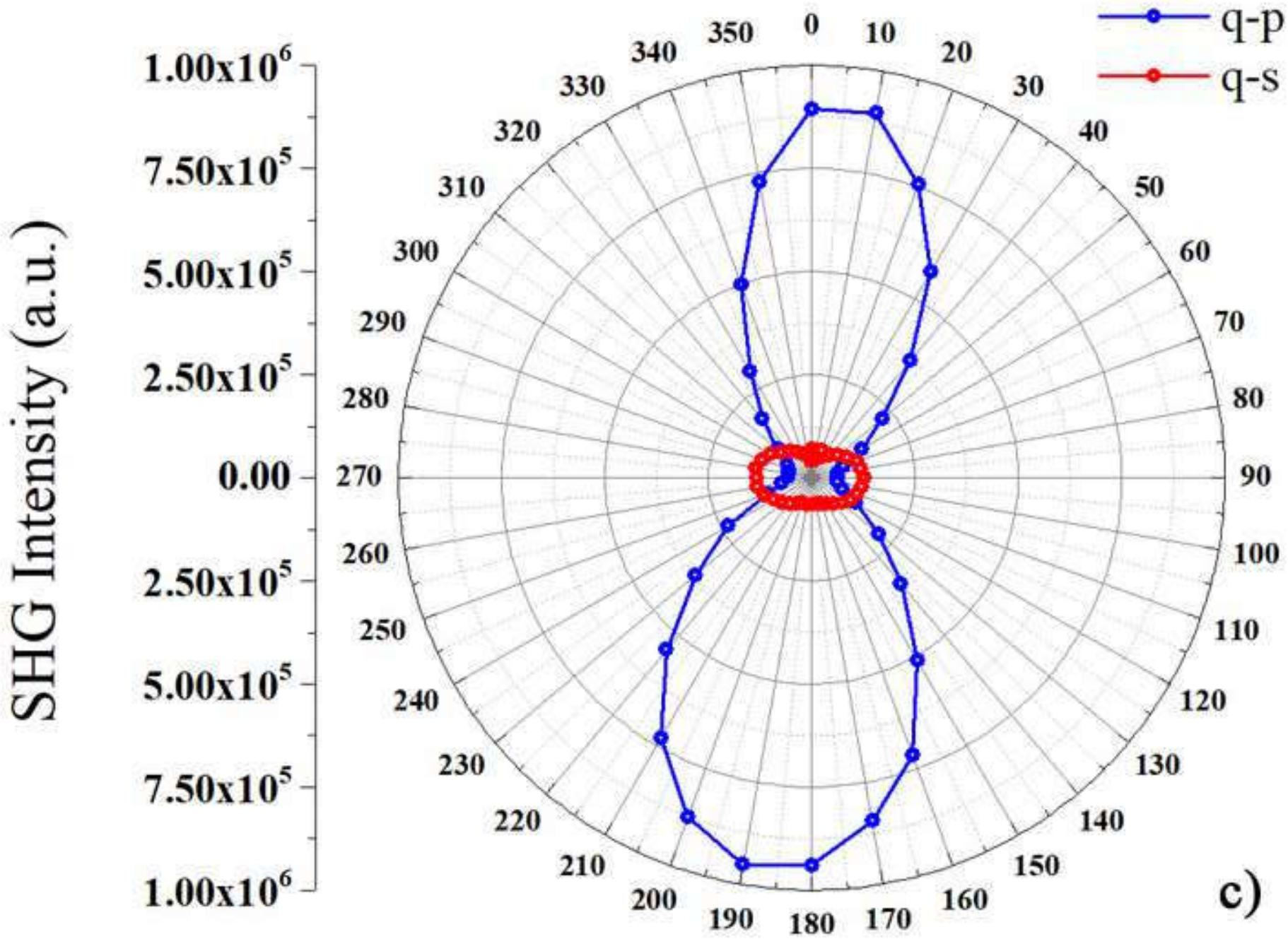

Figure 7d
Click here to download high resolution image

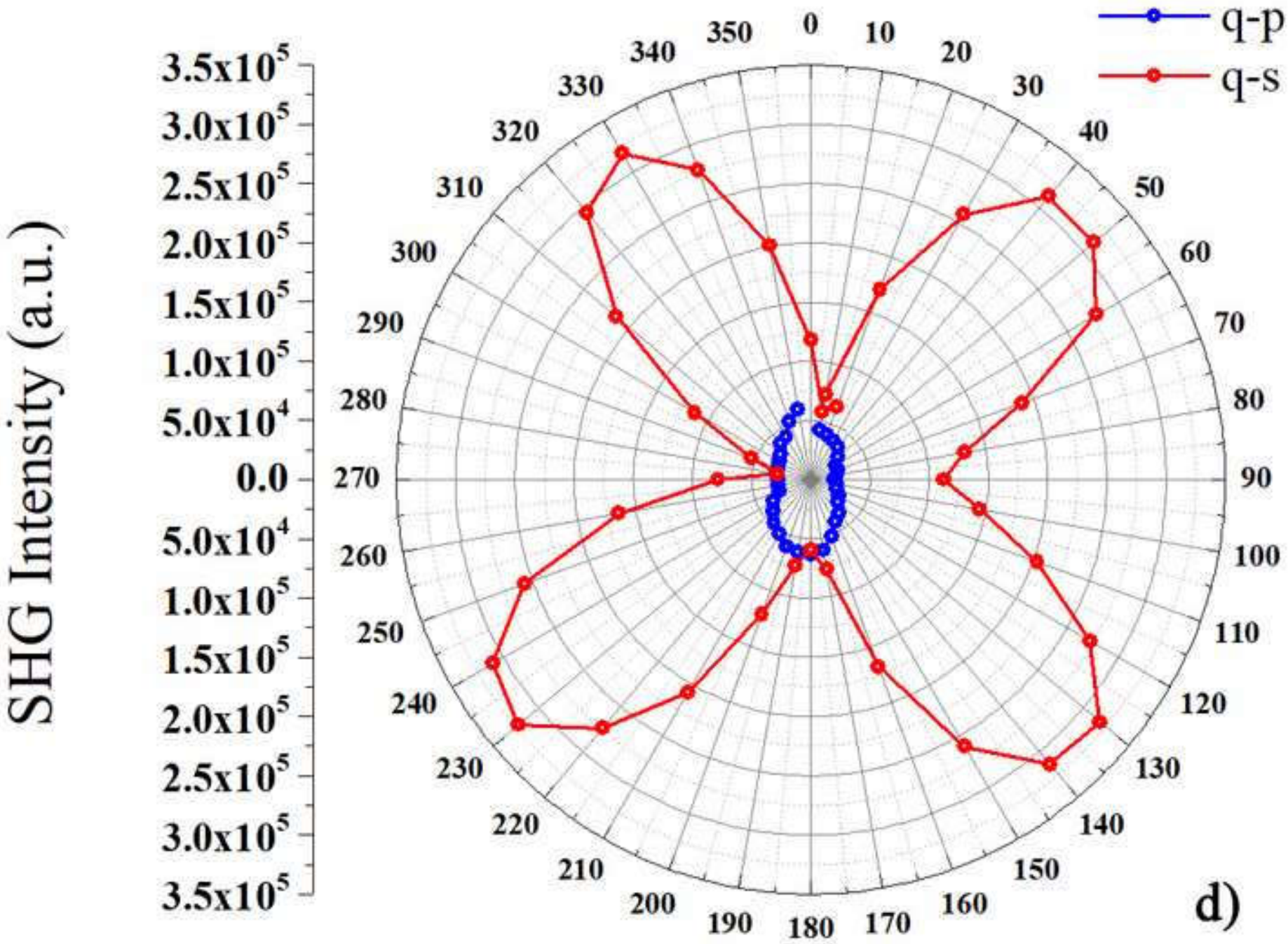

Figure 4a

Click here to download high resolution image

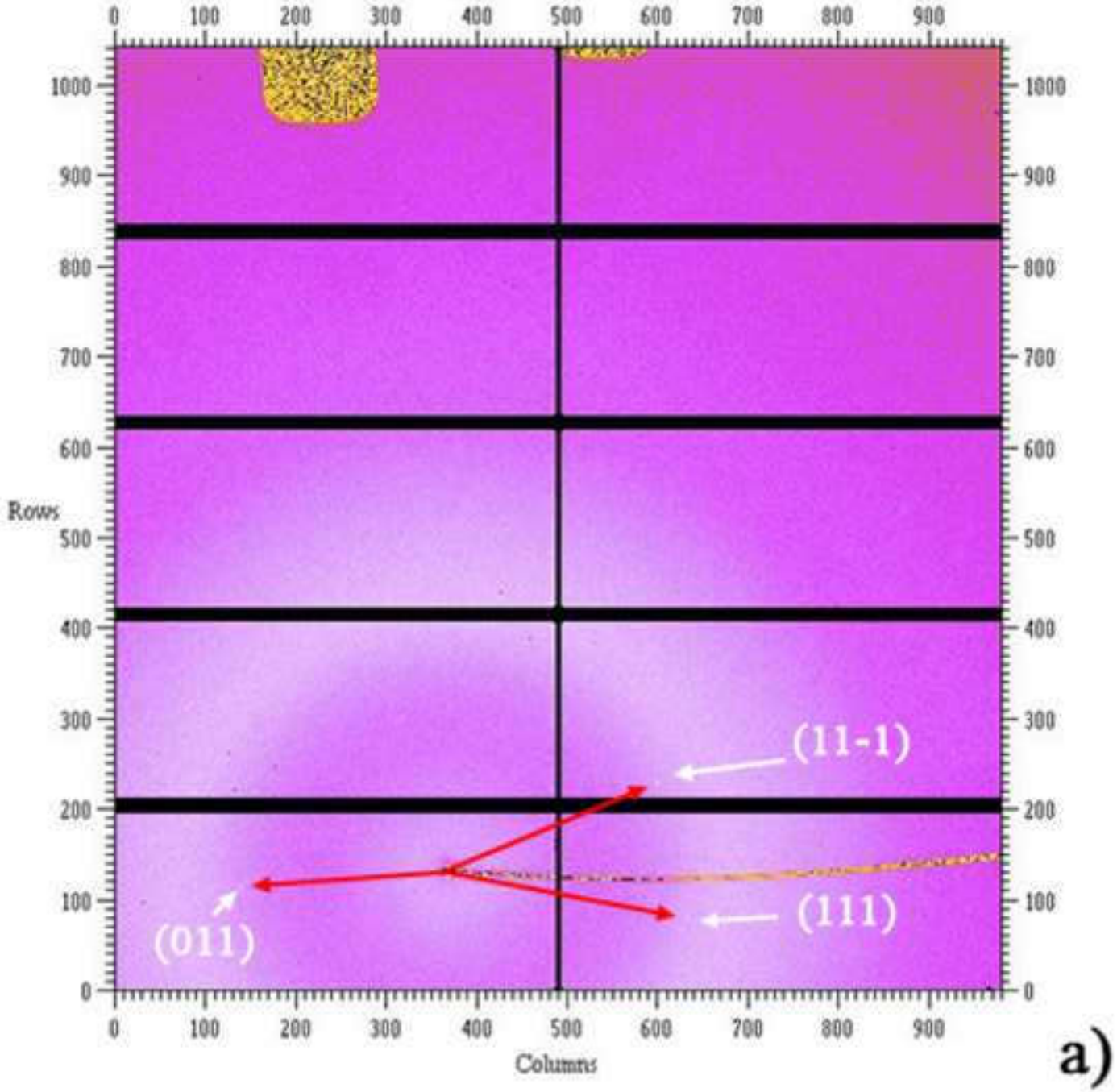

Figure 4b
Click here to download high resolution image

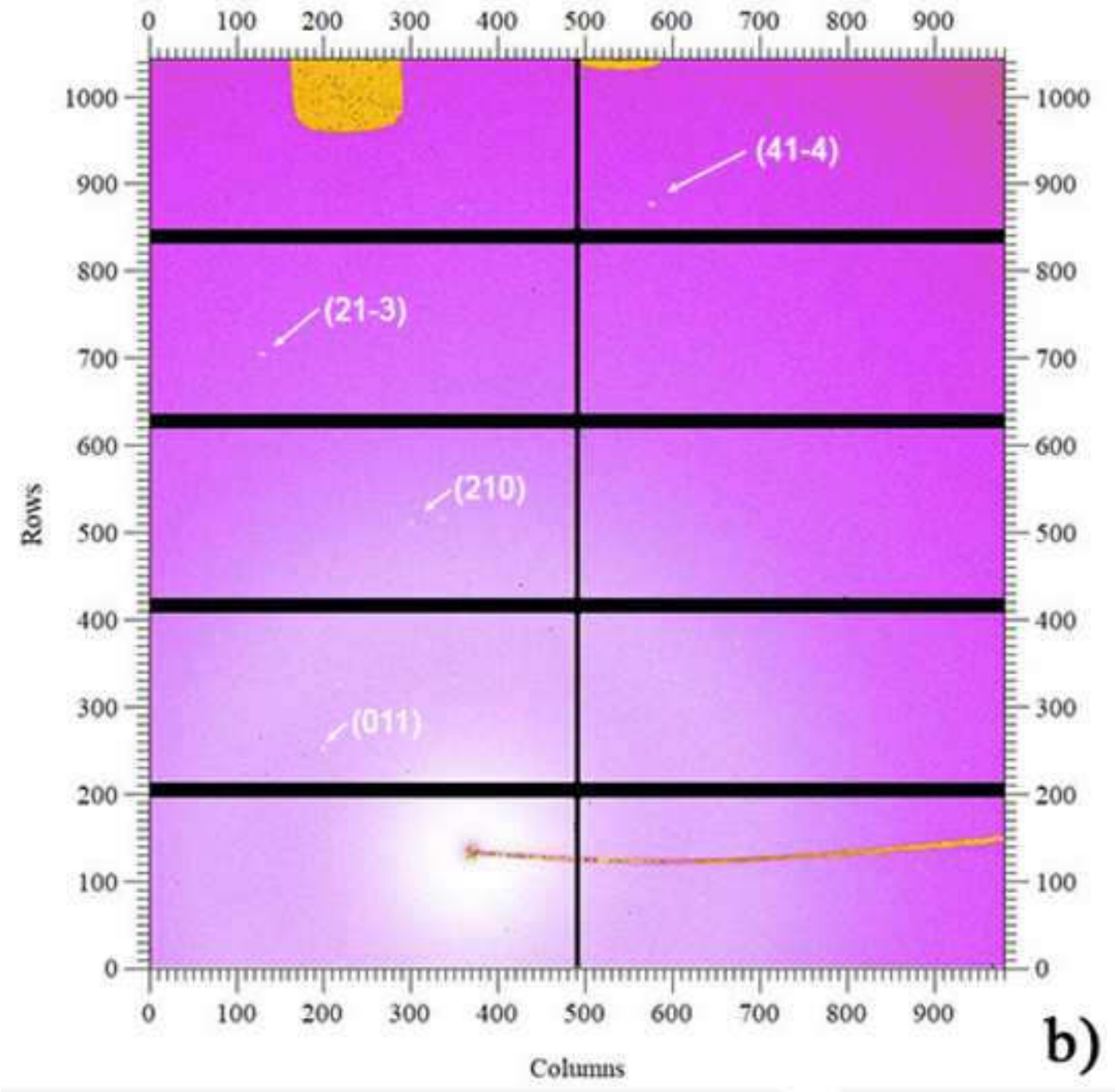

Figure 4c

Click here to download high resolution image

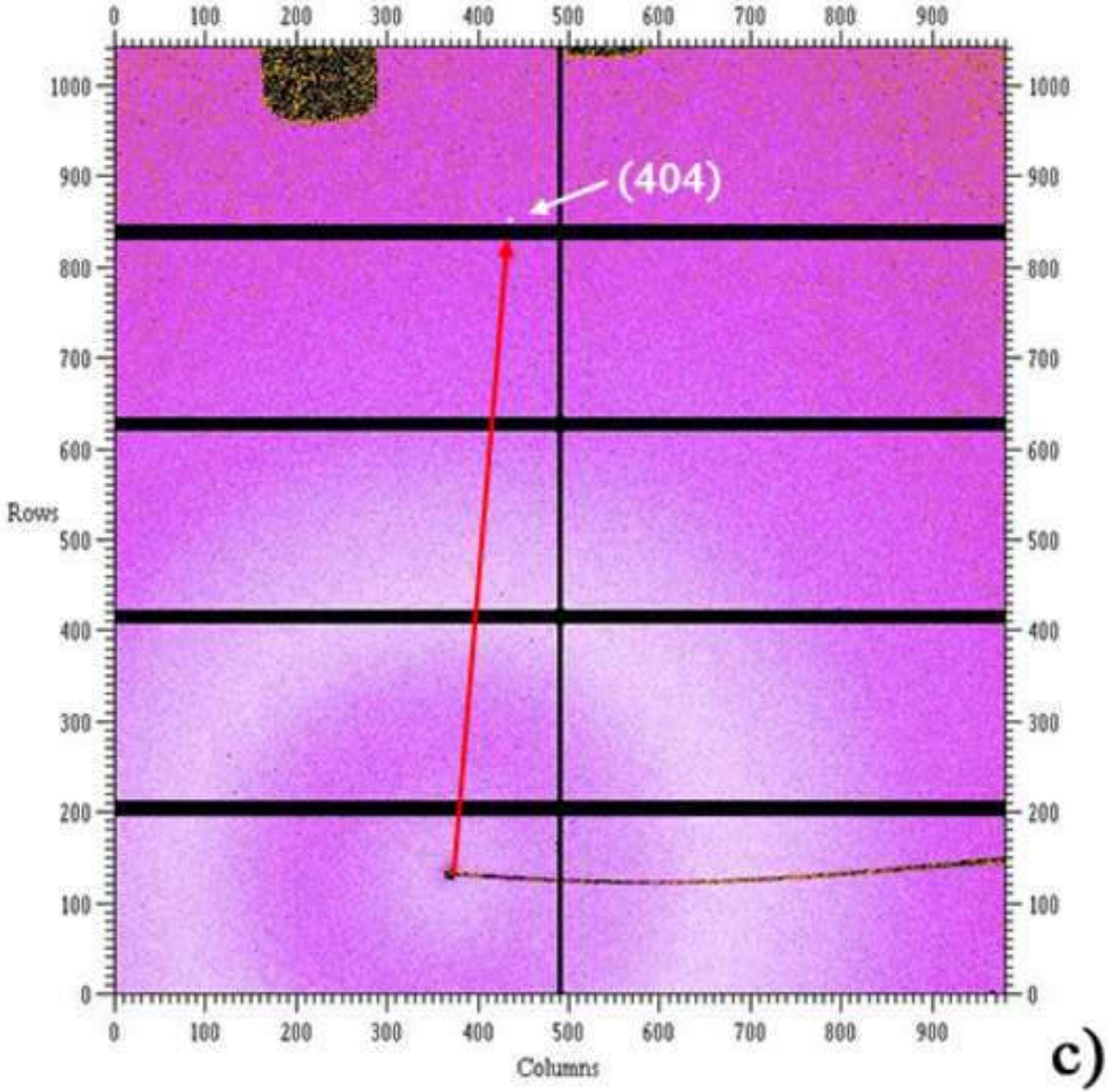

Figure 4d
Click here to download high resolution image